Cloud information from high spectral resolution IR sounders

Kozo Okamoto,[a,b] Anthony P. McNally[a] and William Bell[c]

a. European Centre for Medium-Range Weather Forecasts, Reading, UK
b. Meteorological Research Institute, Japan Meteorological Agency, Tsukuba, Japan
c. Met Office, Exeter, UK

Cloud information from high spectral resolution IR sounders

K. Okamoto, A. P. McNally and W. Bell

This documentation was developed within the context of the EUMETSAT Satellite Application Facility on Numerical Weather Prediction (NWP SAF), under the Cooperation Agreement dated 1 December, 2006, between EUMETSAT and the Met Office, UK, by one or more partners within the NWP SAF. The partners in the NWP SAF are the Met Office, ECMWF, KNMI and Météo France.

Change record			
Version	Date	Author / changed by	Remarks
1.0	28.9.12	K.Okamoto	Version including revisions from A. McNally

Cloud information from high spectral resolution IR sounders

Kozo Okamoto,[a,b] Anthony P. McNally[a] and William Bell[c]

[a]European Centre for Medium-Range Weather Forecasts, Reading

[b]Meteorological Research Institute, Japan Meteorological Agency, Tsukuba, Japan

[c]Met Office, Exeter, UK

Abstract

This paper describes some preliminary investigations of assimilating cloud-affected infrared radiances in general, multi-layer cloudy conditions. Linear estimation theory is used to show that cloudy radiances of the Infrared Atmospheric Sounding Interferometer (IASI) can provide temperature and humidity information inside and even below thin clouds - while this is not possible in opaque overcast cloudy conditions. Including additional cloud variables within the main analysis - with large background errors assigned - can result in temperature and humidity information being aliased in to erroneous cloud adjustments.

An extensive comparison of model first-guess cloudy simulations with observed cloudy radiances shows that 85 (69) % of IASI data over ocean satisfies 10 K (5K) difference of observation-minus-background (O–B) at window channel frequencies. However, there is evidence of a systematic O–B difference corresponding to model cloud deficiencies. The standard deviation (SD) of O–B monotonically increases up to ~ 28 K in the window channels as the magnitude of the cloud effect increases, but then decreases where disagreement between model and observation becomes smaller in overcast conditions. The magnitude of the cloud effect is expressed by a newly developed symmetric parameter ("CA") based upon observed and simulated cloudy radiances. It is found that probability density function (PDF) of O–B departures normalized with a SD predicted by CA exhibits a much more Gaussian form than the PDF normalized with a constant SD.

Using the full ECMWF 4DVAR analysis system, single IASI observation assimilation experiments have been performed. These show that the current assimilation system successfully increases or decreases clouds in line with the O–B radiance departures. However, it is found that the cloud

change is sometimes insufficient (or indeed excessive) and fitting the radiances can be restricted by horizontal resolution and the regularization constraints imposed upon physical processes in the model / assimilation system.

1. Introduction

Progress on the use of cloud- and precipitation-affected radiances at numerical weather prediction centers has been rapid in recent years. The European Centre for Medium-Range Weather Forecasts (ECMWF) assimilates clear-sky, cloud- and precipitation-affected radiances from microwave (MW) imagers ("all-sky assimilation", Bauer *et al.* 2010; Geer *et al.* 2010). However the exploitation of infrared (IR) cloudy radiances is still very conservative – either using data in clear conditions or overcast conditions (McNally *et al.* 2006; McNally 2009). The difficulty in using IR radiances, compared with MW radiances, arises from stronger sensitivity to clouds: the presence of small piece of cloud can significantly decrease brightness temperatures (BTs) by several tens of Kelvins especially at window channels. This generates discontinuous, non-linear response of radiance to cloud variables such as cloud content, fraction and height.

Despite the difficulty in handling IR radiances in the general cloudy situations, several numerical weather prediction centers have been working on assimilation of those radiances. We expect that the most possible approach at ECMWF is extending the already successful path of the MW all-sky radiance assimilation into the IR all-sky assimilation. The merits of using the same approach are fully exploiting lessons learned from MW all-sky assimilation and relatively small changes in program codes.

As our understanding of IR all-sky radiances and their assimilation is limited, the following fundamental questions are arisen:

(1) What information can we obtain from cloudy IR radiances in addition to currently assimilated clear-sky and overcast radiances?

(2) To what extent can current forecast models well simulate cloudy radiance? What is cloud effect on observed and simulated radiances?

(3) Can current assimilation system properly increase or decrease clouds to reduce mismatch between observation and simulation?

This study intends to present preliminary answer to these questions. We used the Infrared Atmospheric Sounding Interferometer (IASI) because of its huge spectrum information and high accuracy. We work on (1) using a linear error analysis to quantify information content of IASI radiances in clear-sky, single-layer cloud and multi-layer cloud scenarios (section 2). Regarding (2), we demonstrate characteristics of cloudy radiance observation, simulations from model first guess (background), and observation-minus-background (O–B) departures. Also, we investigate the variability of O–B as a function of cloud effect and Gaussianity of probability distribution function (PDF) of O–B (section 3). To examine (3), we implement cloudy IASI single observation assimilation experiments using the integrated forecast system (IFS) with the 4D–Var assimilation system at ECMWF (Rabier *et al.,* 2000). Section 4 shows results of five cases. The article concludes with summary and future study in section 5.

2. Linear error analysis of IASI cloudy radiances

2.1 Principle and settings

To quantify information content in IASI spectrum, we calculated error covariance of the optimal state obtained as maximum a posteriori solution assuming a linear system (e. g. Rogers 2000). The error covariance matrix of the optimal state (here we call "analysis") is expressed by

$$\mathbf{A} = (\mathbf{I} - \mathbf{KH})\mathbf{B}, \tag{1}$$

where $\mathbf{B}$ is a background error covariance and $\mathbf{I}$ is an identity matrix. $\mathbf{H}$ is a Jacobian (partial differential) of observation operator, which is a radiative transfer model (RTM) and, if necessary, conversion process of related variables into RTM input variables. We use the radiative transfer model for TOVS (RTTOV) version 10.2 (Saunders et al. 1999; Matricardi et al. 2004) as RTM. $\mathbf{K}$ is called a Kalman gain and written by

$$\mathbf{K} = \mathbf{BH}^T (\mathbf{HBH}^T + \mathbf{R})^{-1}, \tag{2}$$

where $\mathbf{R}$ is an observation error covariance. We examined diagonal components of $\mathbf{A}$ (a_i) and their reduction from $\mathbf{B}$. For quantification of the error reduction, we defined information content at level i (IC_i) as

$$\mathrm{IC}_i = 1 - \sqrt{a_\mathbf{i}} \big/ \sqrt{b_\mathbf{i}} \,. \tag{3}$$

We implemented the linear error analysis in three scenarios: clear-sky case, single-layer cloud case, and multi-layer cloud case. The clear-sky analysis is a reference that gives us basic information of IASI radiances. Analysis variables are temperature (units of Kelvin) and humidity mixing ratio

(g/kg) on 43 pressure levels and skin temperature (T_s, Kelvin). Background states of these variables and other input parameters of RTTOV such as ozone and surface pressure are taken from 27 profiles over sea out of 52 diverse sample profiles the RTTOV package provides. In the second scenario, the single-layer cloud analysis assumes that cloud effect is simply explained by only two cloud parameters of effective cloud fraction F and cloud top pressure P_c. The radiance is calculated with

$$R = F\,R_{ovc} + (1\text{-}F)\,R_{clr}\,, \qquad\qquad (4)$$

where R_{clr} is a clear-sky radiance and R_{ovc} is an overcast radiance emitted from blackbody cloud at level P_c. This equation is too simple to represent real cloud effect, but has some common features to more general RTMs and help us to understand more complex cloud effect. Analysis variables are P_c (hPa) and F in addition to clear-sky analysis variables (87+2=89). In the third scenario, the multi-layer cloud analysis handles general cloud situation such as thin or think multi-layer clouds consisting of liquid and ice condensates. Background cloud profiles are calculated from temperature, humidity and surface pressure based on a large-scale cloud condensation scheme used in 4D-Var linear model (Tompkins and Janisková 2004). Although RTTOV takes into account five different liquid cloud type (three convective and two stratus cloud types) and one ice cloud, we consider only maritime stratus liquid cloud and ice cloud the cloud scheme can provide. Liquid and ice are distinguished by the temperature threshold of 258.15 K. Figure 2.1 shows an example of profiles (the first profile of 27 profiles) of temperature, humidity mixing ratio, cloud water content (C_w, g/m^3), cloud ice content (C_i, g/m^3), cloud water fraction (F_w) and cloud ice fraction (F_i). Analysis variables are C_w, C_i, F_i and F_w on 43 pressure levels in addition to clear-sky analysis variables. Cloud scattering effect in RTTOV is described in Matricardi (2005). We adopted an formulation from Wyser (1998) for ice cloud effective radius and set minimum fraction to 0.001 in the stream method to treat the cloud subcolumn effect, as following the operational setup.

The temperature and humidity elements of **B** are derived from IFS experiments. Although the original humidity analysis variable in IFS is normalized relative humidity (Holms et al. 2002), we converted it into mixing ratio for easier handling and understanding. We assume background error standard deviations (SDs) of T_s, P_c and F are 2.0K, 30 hPa and 0.1, respectively, and that they have no correlations with other variables. **B** of C_w, C_i, F_i and F_w are set to diagonal and their SDs are equal to their own values (100 % relative errors).

For observation, we used a minimum basic channel set or quasi-operational channel set. The basic

channels set contains four channels of 246 (706 cm^{-1}), 1090 (917 cm^{-1}), 2745 (1331 cm^{-1}) 3645 (1556 cm^{-1}). Figure 2.2 (a) and (b) show temperature Jacobian (Jacobians of BT with respect to temperature profile) and humidity Jacobians of the basic channel set for clear-sky case of background profile in Fig. 2.1 (all cloud variables are set to zero). Channel 1090 is sensitive to the surface condition and low tropospheric temperature and humidity. Channel 2745 has similar sensitivity to channel 1090 but weaker peaks at higher altitude. Channel 246 is sensitive to the upper tropospheric temperature and channel 3646 is strongly sensitive to upper tropospheric humidity. The quasi-operational channel set contains 141 channels consisting of the basic channel set plus the operational channels excluding channels with Jacobean peaks above 50 hPa, strong sensitivity to ozone and in short wave band. Temperature and humidity Jacobians of the quasi operational 141 channel set are shown in Fig. 2.2 (c, d). Observation error standard deviation are set to operational values: 1.0 K for stratospheric channels (channel index ≤ 191), 2.0 K for window and humidity channels (≥366), and 0.4 K for others. Non-diagonal components of **R** are ignored.

2.2 Results of the linear error analysis

Figure 2.3 shows SDs of background and analysis errors for temperature and humidity (square root of diagonal components of **B** and **A**). They demonstrate that temperature errors are mainly reduced in the upper and middle troposphere and humidity errors in wide range of troposphere by using IASI radiances. Increasing channels significantly decreases analysis errors of both temperature and humidity in the whole troposphere. This is more clearly seen in IC profiles of temperature and humidity in Fig. 2.4. Many channels sensitive to different levels contribute to increasing ICs at wide levels. The small temperature IC in the lower troposphere comes from large humidity background error and lower tropospheric temperature channels having sensitivity to humidity.

Figure 2.5 (a, b) shows temperature and humidity Jacobians of 141 channel set for a single-layer cloud at P_c=500 hPa with F=1.0. Many channels have sharp and strong sensitivity to the temperature at the cloud. There is no sensitivity to temperature or humidity below the cloud because the cloud completely blocks radiation below it. For F=0.8 in Fig. 2.5 (c,d), the peak of temperature Jacobian at the cloud is smaller and there is non-zero temperature and humidity Jacobian below the cloud. ICs of temperature and humidity below the cloud are smaller in the single-layer cloud case than those in clear-sky cases, shown in Fig. 2.6, due to the decreasing Jacobians. One may feel strange that temperature ICs at the cloud height are very small despite strong peak of the

temperature Jacobian. This is attributed to large background errors of P_c and F (30 hPa and 0.1), temperature and humidity increment being easily aliased into cloud increment. When we set smaller background errors of cloud (3 hPa and 0.01), temperature IC at the cloud and humidity IC below the cloud significantly increase (blue and green lines in Fig. 2.6). By contrast, the ICs of P_c and F are smaller for smaller cloud background errors (for example, IC is reduced from 0.691 to 0.109 for F=1.0, and 0.406 to 0.016 for F=0.8).

In multi-layer cloud profiles shown in Fig. 2.1, Jacobians with respect to temperature, humidity, C_w, C_i, F_i and F_w are plotted in Fig. 2.7. The temperature Jacobians of lower tropospheric and window channels have small peaks in the upper part of cloud that does not appear in clear-sky cases while humidity Jacobians does not differ so much. This small change in Jacobians is the effect of small cloud content and fraction. For a dense cloud, the Jacobians become similar to those in single-layer cloud case. Cloud Jacobians in Fig 2.7 (c) ~ (f) are localized at layers in the presence of clouds. Please note that cloud content Jacobian is the most sensitive to the upper part of cloud (Fig 2.7 (c, d)) while cloud fraction Jacobian peak is at a level of maximum cloud fraction (Fig 2.7 (e, f)) or at a little upper level (e.g. for the eighth profile, not shown). Figure 2.8 shows that there is temperature and humidity ICs even inside and below cloud although they are smaller than ICs in the clear case. ICs of C_w and F_w are obtained at layers where liquid cloud is while there is almost no IC of ice clouds due to too few ice cloud and then small C_i and F_i Jacobians. For denser clouds, we can obtain greater ICs from ice cloud due to increasing Jacobians unless the sensitivity increase saturates (not shown).

IC is expected to vary for different background profiles. We compared ICs of all 27 profiles. To make the comparison easier, we combined water and ice clouds and created a new measure of total IC (TIC) by accumulating ICs at all levels. Figure 2.9 (a) shows that humidity TIC is much greater than other TICs for almost all profiles. Cloud TICs (both content and fraction) are smaller than temperature and humidity TICs for most profiles. Profound exception is that cloud fraction TIC is larger than temperature TIC in the profile 12, 16 and 19 that have large F. Figure 2.9 (b) shows the ratio of TIC with 141 channels over TIC with 4 channels. The ratios of all variables are over 1.0 in all profiles, illustrating that increasing channels multiplying TIC, except for cloud variables in the profile of 4, 13 and 27 that have no clouds in the background. The increasing ratio of temperature TIC is significantly greater than others. In contrast, the ratio for cloud TICs is smaller than for the

other variables at almost all profiles. This is probably attributed to the small variability of peak height and shape of cloud Jacobians from channel to channel, leading to difficulty in gaining new information by additional channels. Please note that in a real assimilation system, even a small cloud change can make a big difference in RT calculation, and then affect analysis of all related variables, as will be shown in section 4.

As the final remarks in this section are, because an inversion process of RTM allows many possible solutions, assimilating radiance data with insufficient information can sometimes cause spurious increments arising from large uncertainty of the likelihood of a state. For example, when assimilating radiance data with negative O–B, we will seek the most likelihood state by decreasing temperature, or increasing humidity, cloud content or cloud fraction. Figure 2.9 shows that the uncertainty of all variables, especially humidity, is reduced by assimilating IASI radiances, and that the magnitude of the uncertainty reduction becomes greater with more channels used.

3. Characteristics of IASI cloudy radiances

3.1 Simulation of cloudy IASI radiances

To understand how well models (forecast model and RTM) simulate IASI cloudy radiances, we examined characteristics of observations, first-guess (FG) and O–B BTs. We performed passive assimilation cycles from 1 through 31 August 2011. This passive cycle assimilated all operational data except IASI radiances. The assimilation system employed was a reduced resolution version of the operational system as of July 2012 (38r1) where spectral resolution was T511 (~40 km) and 91 levels in the vertical up to 0.01 hPa. IASI pixels were globally thinned to 1/30, instead of the operational setting of 1/3, to avoid memory shortage problems. RTM used was RTTOV version 10.2, as in section 2. O–B departures were taken before bias correction because operational bias correction coefficients were created based on clear-sky radiance samples using a variational bias correction (VarBC) scheme and it was found that they tended to make O–B slightly positive for all-sky radiances. The data over sea-ice and land were excluded when statistics were calculated except for geographical maps. All the plot and statistics in this section were made from the data taken from 1 to 13 August 2011 except for a geographical map and a look-up table of O–B SD, as will be explained later.

3.2 Comparison of observation and simulation

Figure 3.1 shows density scatter plots of observation and simulation at channels 246, 1090 and 3645. On the whole, simulations agree with observations: 85 (69) % of all data satisfy |O–B| < 10K (5K) over the sea at channel 1090 that is the most sensitive to cloud. However, the simulation at channel 1090 has fewer populations than observations at low BT (BT < 260 K). In addition the samples at BT~290K are more present in simulation than in observation. Figure 3.2 shows PDFs of O–B, together with clear-sky O–B that was given by turning off cloud scattering effect in RTTOV. While clear-sky O–B presents highly asymmetric, strongly negative tailed O–B PDFs, all-sky O–B PDFs show much more symmetric. Nevertheless, negative tail is slightly evident especially at channel 1090, corresponding to smaller samples of low BT simulations described above.

A geographical map of O–B monthly mean at channel 1090 shows that this disagreement reflects model deficiency in cloud (and humidity) representation (Fig 3.3). A systematic negative O–B can be seen in storm track and stratocumulus regions off the west coast of the South America and the South Africa. It is known that model underestimate clouds in these regions at ECMWF (for example, Kohler *et al*. 2011 for the stratocumulus). A systematic positive O–B area is seen in subtropical regions in the Southern Hemisphere, corresponding to overestimation of model clouds. The relationship between deficiency in model cloud representation and systematic O–B can be confirmed by similar (but opposite signed) O–B patterns seen in all-sky MW imagers (not shown). Figure 3.4 illustrates that SD of observation is much smaller than SD of simulation especially in the Intertropical Convergence Zone (ITCZ). We speculate that this is mostly caused by the lack of high clouds in the model and detailed investigation is future issue.

3.3 Cloud effect on O–B statistics

Figure 3.5 shows O–B SD and mean (bias) when the cloud scattering calculation is turned off and on in RTTOV at all 373 channels that ECMWF receives from EUMETSAT. Channels sensitive to clouds have large SD and negative bias in clear-sky calculation, but including the cloud scattering effect in RTTOV significantly reduces both SD and bias. However, even after including the cloud scattering effect in RTTOV, there still remains SD of 9.5 K and bias of -2.5 K at window channels. Also, we suppose that these values vary much according to meteorological conditions as shown in Figs. 3.3 and 3.4.

To express cloud effect, it may be straightforward to use directly cloud-related traditional parameters such as cloud fraction and cloud top height. However, retrieving these cloud parameters is sometimes difficult for thin, multilayer cloud cases and what we exactly need is the extent cloud affects radiance rather than cloud property itself. Furthermore, given highly varying cloud effect from channel to channel, it is beneficial to use a highly channel dependent parameter Thus, we developed a new parameter called cloud effect average (CA) .

$$CA = (|CM|+|CO|)/2, \qquad (5)$$

CM and CO are cloud effect for model and observation, respectively, written by

$$CM = B - B_{clr}$$

$$CO = O - B_{clr}$$

B_{clr} is clear-sky background BT when the cloud scattering calculation is switched off in RTTOV. CA increases as observation and all-sky background differ from B_{clr} (for example, cloud fraction or height increase). In contrast CA equals zero when O ~ B ~ B_{clr}. The reason why we use both CM and CO as CA, instead of using either only CM or only CO, is to create a 'symmetric' parameter, following the recommendation by Geer and Bauer (2011). The symmetric parameter allows us to avoid a sampling issue that happens if we identify cloudy data or estimate cloud effect based on model or observation information only, as will be shown later.

Figure 3.6 shows density scatter plots of O–B as a function of CA, CM and CO at channel 1090. As CA becomes large, O–B variability increases and then becomes small. The CA region with declining O–B variability represents overcast conditions where model relatively better simulates clouds. In contrast to the distribution with CA, the distributions with CO and CM are asymmetric about O–B = 0. O–B SD and mean calculated from samples binned as a function of CA at channels 246, 1090 and 3645 are plotted in Fig. 3.7. SDs monotonically increases with CA and declines after they reach the maximum values that are different for channels or cloud sensitivity. This SD change with CA is similar to all-sky MW as a function of symmetric mean cloud parameter (Geer and Bauer 2011). The simple relationship between O–B SD and CA suggests that CA can be a good parameter to predict O–B SD. O–B mean is almost constant for most samples at channel 246 and monotonically decreases at channel 3645. In contrast, O–B mean at channel 1090 slightly increases at small CA and then quadratically decreases at higher CA. Moreover O–B means at all of these channels take parabolic curves in the positive O–B side at the highest CA although the variability is large due to small samples. The investigation of mechanism explaining the O-B mean change with

CA is future issue and will help us develop VarBC predictors using CA. It is found that there is almost no dependence of O–B SD and mean on scan angle (not shown).

The importance of properly including cloud effect can be seen in PDF of O–B. Figure 3.8 shows PDFs of O–Bs normalized by the SD of whole sample (constant SD irrespective of cloud effect, blue curves), and those normalized by the SD binned as a function of CA (cloud-dependent SD, red curves). PDFs by ignoring cloud effect have too narrow peaks and wide tails because the constant O–B SD (2.68, 9.60 and 2.63 K for channels 246, 1090 and 3645) is larger (smaller) for small (large) O–B than it should be seen in Fig 3.7. In contrast, PDFs by including cloud effect become much closer to Gaussian distribution (green). As Geer and Bauer (2011) suggest, the O–B normalized by cloud-dependent O–B SD can also be used for a quality control (QC) procedure that test if data with large O–B are reasonably affected by clouds or contaminated by other unexpected factors. However, channel 3645 is less fit to Gaussian (Fig 3.8(c)) probably because the channel is enormously affected by upper tropospheric humidity too. Thus, for channels greatly sensitive to other elements than cloud such as humidity and ozone, the dependency of O–B SD on all of these elements must be considered. Otherwise, we may need to give up using those channels. If we use an 'asymmetric' parameter for the cloud effect, PDFs of normalized O–B do not fit Gaussian as a result of unbalanced sampling (Fig. 3.9). Too wide tail in the O–B positive side is the result of small O–B variability in positive O–B area as CO magnitude increases (Fig. 3.6 (b)).

3.4 Predicting O–B SD

We now know that the cloud effect parameter CA well explain the variation of O–B SD. Because O–B SD can be used for a QC parameter and observation error calculation, predicting O–B SD with CA is very beneficial for assimilating cloudy data. Geer and Bauer (2011) developed a simple linear function with their symmetric cloud parameter to predict O–B SD. However, our attempt to fit O–B SD with a linear or quadratic function of CA at both small and large CA was not successful. Accordingly, we determined to adopt a pre-calculated look-up table (LUT) at 100 bins of CA to give O–B SD, instead of using higher order fitting functions. There is a caveat of creating the LUT at all channels: For samples that are not affected by clouds, $|O–B| \sim 2*CA$ since $B \sim B_{clr}$. In this case O–B SD is too close to zero for a bin at small CA to be practically useless for our purpose. One example of this problem at channel 179 (sensitive to the upper tropospheric or stratospheric temperature) is shown in Fig. 3.10 (a), where excessively small O–B SD produce double a peaked

PDF. To avoid this, we set the minimum O–B SD to a value calculated from only clear-sky samples. Fig. 3.9 (b) shows this treatment works well.

We made the LUT of O–B SD against CA at 373 channels using the data over sea from August 16 through 31 2011. O–B SD was calculated at 100-binned CA and smoothed using contiguous bins. The value calculated from clear-sky samples was provided with bins where original O–B SDs were too small, as early described. At large CA bins where O–B SDs declined with CA, we fit a linear function to avoid missing bins due to few samples. O–B SDs with CA in the LUT are plotted at all 373 channels in Fig 3.11. O–B SDs of cloud-affected samples are much larger than observation errors assigned for the operationally used clear-sky and overcast samples, put with parenthesis above each panel of the Fig 3.11. O–B SDs at window channels have a wide CA range and reach as high as 28 K (Fig 3.11 (c)). For the stratospheric channels, both CA range and SDs are smaller than other channels (Fig 3.11 (a)). As for short wave channels, O–B SD reaches 35 K probably due to the contamination by daylight in addition to cloud effect (Fig 3.11 (h)). To confirm the validity of the LUT, we compared PDF of O–B normalized by their own O–B SD (Fig. 3.8) with the one normalized by O–B SD predicted from the LUT that was created from different samples. They agreed very well (not shown), justifying the LUT to be used to predict O–B SD of independent samples.

3.5 Treatment of cloud inhomogeneity

Although RTTOV calculates radiative transfer in sub-grid columns determined by model cloud fraction and maximum-random overlap assumption (Matricaldi 2005), it is difficult to accurately simulate radiances strongly affected by inhomogeneous, partial clouds. It would be wise to screen out inhomogeneous pixels if we can efficiently identify them. IASI dataset disseminated by EUMETSAT contains cloud information based on a cluster analysis of collocated Advanced Very High Resolution Radiometer (AVHRR) data (Cayla F. 2001). It includes mean and SD of AVHRR radiances at six channels and fraction of each cloud cluster. ECMWF converted these cluster-based statistics into IASI pixel-based statics such as an average of the radiance means and SDs with the weight of the cluster fraction, and radiance of the coldest, warmest or largest cluster. It was found that the averaged AVHRR SD (SD_{AVHRR}) was a good indicator of cloud inhomogeneity.

Figure 3.12 shows O–B PDFs and observed BTs at channel 1090 of all samples over the sea and

samples that satisfy SD_{AVHRR} < 3 or 1 (mW/m^2/sr/cm^{-1}). This inhomogeneity screening reduces negative tails of O–B, making PDFs more symmetric compared with PDF of all samples (Fig.3.12 (a)). However, it reduces more samples at low BT than those at high BT (Fig. 3.12 (b)), indicating that the inhomogeneity screening is likely to remove high cloud samples and keep low cloud or clear-sky samples. A stricter screening of SD_{AVHRR} < 1 further excludes low BT samples and slightly shifts O–B PDF to the positive side. Therefore we need to know that rejecting inhomogeneous data simply by applying a strict screening test may prioritize low cloud and clear-sky data although negative PDF tails are reduced. Thus, the best option is to exclude extremely inhomogeneity data only, and allow modestly inhomogeneous data to be used with large observation errors (large representative error). In fact, the stricter the screening test, the smaller O–B SD (Table 3.1). This result may suggest that O-B SD LUT should vary with not only CA but also the inhomogeneity in future.

4. Assimilation experiment with single observation

4.1 Methods

To examine whether cloudy IASI radiance assimilation properly correct FG cloud fields in the operational data assimilation system, we implemented assimilation experiments with single IASI observation. We used a reduced resolution version of the operational data assimilation system (T511L91) as of July 2012 (cy38r1). It employs incremental 4D-Var with 12-hour time window and performs three inner-loop minimizations at spectral resolution of T95, T159 and T255 (approximately 210 km, 125 km and 80 km, respectively) corresponding to three outer-loop updates. Analysis variables in the ECMWF 4D-Var are related to the temperature, wind, surface pressure, ozone and humidity. Cloud variables, such as cloud water (ice) content and cloud fraction, are not directly analyzed: Their analysis increments are generated from temperature and humidity perturbations through moisture processes in the 4D–Var linearized models (large-scale condensation and convective schemes; Tompkins and Janisková 2002; Lopez and Moreau 2005). Please note that the cloud scheme of nonlinear forecast model includes cloud liquid water, cloud ice and cloud fraction in prognostic variables.

To clarify the impact of IASI cloudy radiances, we performed baseline experiments where no satellite data (only conventional data) were assimilated, hereafter called "CNTL", and then performed "TEST" experiments by adding single pixel of IASI to CNTL configuration. We choose

five cases for the analysis at 00 UTC on 1 June 2012, according to O–B, observation time, diagnosed cloud top height P_c and effective fraction F_e of IASI data. The diagnosed cloud information is derived to minimize the radiance difference between observation and single-layer blackbody overcast simulation (McNally 2009). Since cloudy radiances can have much larger O–B than clear-sky radiances, they could be rejected by FG check or significantly down-weighted by Variational QC (VarQC) in the operational system. To avoid this, we deactivated these QC procedures by setting extremely relaxed criteria. Tuning QC parameters based on the cloud-dependent O–B SD predicted by the LUT should be better treatment, as described in section 3, and the implementation will be considered in future. Observation errors were assigned to 1 K for channel 101 and 3 K for other channels when we assimilated seven channels (101, 246, 272, 921, 2889 and 3110). In addition, we assimilated 138 channels having observation errors of O–B SD given by the LUT in section 3. The 138 channels were the same channels used in section 2 excluding channels 1090, 2745 and 3645 that were not in the operational channel set. Table 4.1 shows specification of the five experiments.

4.2 Results of single observation experiments

Figure 4.1 shows (a,b,c) profiles of FG and analysis of cloud water content (C_w), cloud ice content (C_i) and cloud fraction (F) in TEST, CNTL, TEST–CNTL, and (d) O–B and observation-minus-analysis (O–A) in the BT space in TEST and CNTL for case 1 experiment. O–B at most channels is positive, which means excessive clouds in FG than in observation. O–A in both CNTL and TEST is larger than O–B but O–As in TEST is smaller than O–As in CNTL. This indicates that conventional data increase clouds but IASI suppresses the increase. It can be seen in the reduction of F at the cloud top and bottom and in C_i in the whole high cloud. One would expect that if F is further reduced, especially at levels of $F = 1$, O–A would be further reduced. But F increment is limited when F is close to 1 due to the regularization process incorporated in linear model physics. The regularization smoothes the discontinuities in physical schemes in order to make the model as much differentiable and stable in minimization as possible (Janiskova and Lopez 2012). F perturbation generated in the linearized large scale condensation process is significantly suppressed as F approaches one by multiplying correction coefficient (0.2 for $F > 0.7$ and almost 0 for $F > 0.95$). In contrast, this treatment allows F correction by analysis only when F is far from 1.0. This can be clearly seen in case 2 experiment. Case 2 shows the lack of model clouds, which is confirmed by negative O–B (Fig. 4.2). Both cloud content and fraction are significantly increased in the middle

troposphere by IASI assimilation, significantly reducing O–A except humidity channels (channel index $\geq$ 2889). This involves a large temperature increment more than 3 K (not shown) because the constraint is small due to no other satellite observations and the use of large IASI O–B is allowed due to relaxed QC.

In contrast to case 2, case 3 demonstrates negative O–B and positive O–A by excessively increasing clouds in TEST run (Fig 4.3). A close look at the change in cloud profiles at each updated outer-loop trajectory reveals that C_i is substantially increased in the first updated trajectory but decreased in the final trajectory (Fig4.4). Also F of the uppermost cloud is slightly reduced from the first trajectory to the final trajectory. This suggests that the excessive response of cloud generation was related to some deficiencies in the first inner-loop minimization or outer-loop update. For example, coarse horizontal resolution may cause unrealistic trigger of moist process in the inner-loop. Spurious behaviors in the minimization process could be alleviated by increasing horizontal resolution, iteration number of each minimization and outer-loop update. Bauer et al (2011) also discussed discontinuity in updated trajectories for their MW all-sky assimilation and severely problematic situations could be avoided by FG checks and VarQC.

Figure 4.5 shows a more complicated situation in case 4 where upper tropospheric channels have positive O–B and lower tropospheric channels negative O–B. One would expect that the system decreases high cloud and increases middle or low clouds. F increment shows a modestly expected change of reduced clouds around 200 hPa and increased clouds around 500 hPa (Fig 4.5 (c)). However, analysis BT increases at all channels and O–A of most channels has larger negative values probably because the reduced high cloud increases radiation at the top of atmosphere even for lower tropospheric channels. This case indicates the difficulty in finding a good balance for all channels using only IASI observations.

It is interesting to examine overcast cases where the operational system already assimilates radiances when F_e > 0.99 over the ocean (McNally 2009). For case 5, all-sky radiance assimilation successfully increases cloud, shown in Fig.4.6. Furthermore, surprisingly, it moves the cloud up to the level corresponding to diagnosed cloud top (P_c = 666 hPa) although analyzed F_e is not sufficient compared with diagnosed fraction (0.7 vs 0.994), probably due to the restriction on supersaturated increment (not shown). This encouraging result suggests the possibility that the all-

sky approach is able to reasonably include current overcast assimilation.

We have shown that the all-sky radiance approach can overall properly increase or decrease clouds according to O–B in a single observation experiment context. However there are some technical problems with IR radiances calculation in the all-sky approach. For example, minimization sometimes failed when we tried to assimilate 138 channels with the operational observation errors that were smaller than those given by the O–B SD LUT. This failure occurred due to insufficient accuracy of adjoint calculation (relative error of adjoint test is 5 %). This problem is not so serious as to change or deny the results we have shown here, but this does not mean we can ignore it. In addition, forward calculation of IR cloudy radiance in RTTOV requires huge memory consumption. In this study we took an ad-hoc measure of significantly thinning IASI observations (1/30), as stated in section 3. We need to resolve these technical problems to make further investigation and conduct full data assimilation experiments.

5. Conclusion

This study conducted basic research on the IR radiance assimilation in general cloudy situations. Regarding three questions we raise in the introduction, the answers obtained from this study are as follows:

(1) Temperature and humidity information can be obtained inside and below clouds if the clouds are thin. Cloud information (height, content and fraction) can also be obtained by treating them as analysis variables. However, the temperature and humidity information obtained is limited if cloud analysis variables with large background errors are defined.

(2) The current model overall well simulates cloudy radiance over the ocean with 85 (69) % of all data satisfying |O–B| ≤ 10 (5) K at window channel. O–B SD monotonically increases up to 28 K at window channels as cloud effect rises, and then declines in overcast condition. Appropriately represented cloud effect, which is "CA" newly developed in this study (Eq.5), is important to properly sample cloud-affected data and predict observation errors and QC parameters.

(3) The current assimilation system overall properly increases or decreases clouds according to O–B of assimilated IASI channels. However technical and physical constraints such as regularization, restriction on supersaturation and coarse inner-loop resolution sometimes does not allow the system to change clouds so that O–A is much smaller than O–B.

There are many important issues that this study does not cover. The minimization performance due to non-linearity of cloud processes should be carefully investigated. We may need to remove data causing high-nonlinear problems or alleviate non-linearity by averaging neighboring pixels with similar cloud characteristics. The selection of more appropriate channels related to cloud variables may be necessary because current channel selection basically intends to gain as much information as possible in clear-sky conditions (Collard 2007). Developing and tuning QC parameters, bias correction predictors and observation errors taking into cloud effect are also inevitable. Regarding the inhomogeneity screening discussed in section 3, it is important to find best balance of inflation factor of observation errors and screening threshold.

Acknowledgements

References

Bauer P, Geer AJ, Lopez P, Salmond D. 2010. Direct 4D-Var assimilation of all-sky radiances. Part I: Implementation. *Q. J. R. Meteorol. Soc.* **136:** 1868–1885.

Collard, AD. 2007. Selection of IASI channels for use in numerical weather prediction. *Q. J. R. Meteorol. Soc.* **133**: 1977–1991. doi: 10.1002/qj.178

Cayla F. 2001. '*AVHRR radiances analysis inside IASI FOV's,*' CNES internal report (IA-TN-0000-2092-CNE). CNES: Toulouse, France.

Geer, AJ, Bauer, P, Lopez, P. 2010. Direct 4D-Var assimilation of all-sky radiances. Part II: Assessment. *Q.J.R. Meteorol. Soc.*, **136**: 1886–1905. doi: 10.1002/qj.681

Geer, AJ, and Bauer, P. 2011. Observation errors in all-sky data assimilation. *Q. J. R. Meteorol. Soc.* **137**: 2024–2037. doi: 10.1002/qj.830.

Hólm EV, Andersson E, Beljaars A, Lopez P, Mahfouf J-F, Simmons A, Thépaut J-N. 2002. 'Assimilation and modelling of the hydrological cycle: ECMWF's status and plans'. Tech. Memo. 383, pp. 55.

Janisková M, Lopez P. 2012. 'Linearized physics for data assimilation at ECMWF'. ECMWF Tech. Memo. 666, pp. 26.

Lopez P, Moreau E. 2005. A convection scheme for data assimilation: Description and initial tests. *Q. J. R. Meteorol. Soc.* **131**: 409–436.

Köhler, M., Ahlgrimm, M. Beljaars, A. 2011. Unified treatment of dry convective and stratocumulus-topped boundary layers in the ECMWF model. *Q.J.R. Meteorol. Soc.*, **137**: 43–57. doi: 10.1002/qj.713

Matricardi M, Chevallier F, Kelly G, Thépaut J-N. 2004. An improved general fast radiative transfer model for the assimilation of radiance observations. *Q. J. R. Meteorol. Soc.* **130**: 153–173.

Matricardi M. 2005. 'The inclusion of aerosols and clouds in RTIASI, the ECMWF fast radiative transfer model for the infrared atmospheric sounding interferometer'. ECMWF Tech. Memo. 474, pp. 53.

McNally AP, Watts PD, Smith JA, Engelen R, Kelly GA, Thépaut J-N, Matricardi M. 2006. The assimilation of AIRS radiance data at ECMWF. *Q. J. R. Meteorol. Soc.* **132**: 935–957.

McNally AP, 2009. The direct assimilation of cloud-affected satellite infrared radiances in the ECMWF 4D-Var. *Q. J. R. Meteorol. Soc.* **135:** 1214–1229.

Rabier F, Järvinen H, Klinker E, Mahfouf JF, Simmons A. 2000. The ECMWF operational implementationof four-dimensional variational assimilation. I: Experimental results with simplified physics. *Q. J. R. Meteorol. Soc.* **126**: 1148–1170.

Rodgers CD. 2000. *Inverse methods for atmospheric sounding: theory and practice.* World Scientic: Singapore.

Saunders R, Matricardi M, Brunel P. 1999. An improved fast radiative transfer model for assimilation of satellite radiance observations. *Q. J. R. Meteorol. Soc.* **125**: 1407–1426.

Tompkins AM, Janisková M. 2004. A cloud scheme for data assimilation: Description and initial tests. *Q. J. R. Meteorol. Soc.* **130**: 2495–2517.

Wyser, K. 1998. The effective radius in ice clouds. *J. Clim.*, **11**, 1793–1802.

Table 3.1 The number, O–B mean and O–B SD of data before and after inhomogeneity screening with different thresholds of AVHRR radiance SD.

	all	$SD_{AVHRR} < 3$	$SD_{AVHRR} < 2$	$SD_{AVHRR} < 1$
number	84,560	58,091	46,707	31,826
O-B mean	-1.84	-0.99	-0.72	-0.20
O-B SD	9.60	7.98	7.37	6.01

Table 4.1 The location, time, number of channels and diagnosed cloud top pressure (P_c) and effective cloud fraction (F_e) of observation assimilated in five single-observation experiments.

	lat, lon	time	number of channels	diagnosed P_c, F_e
case 1	4.52N, 87.74W	3:35	138	256hPa, 0.97
case 2	0.36N, 16.28W	22:30	138	443hPa, 0.74
case 3	7.00N, 132.07E	01:00	7	289hPa, 0.77
case 4	9.22N, 147.93E	23:18	138	186hPa, 0.95
case 5	51.02N, 158.53W	21:24	138	666hPa, 0.992
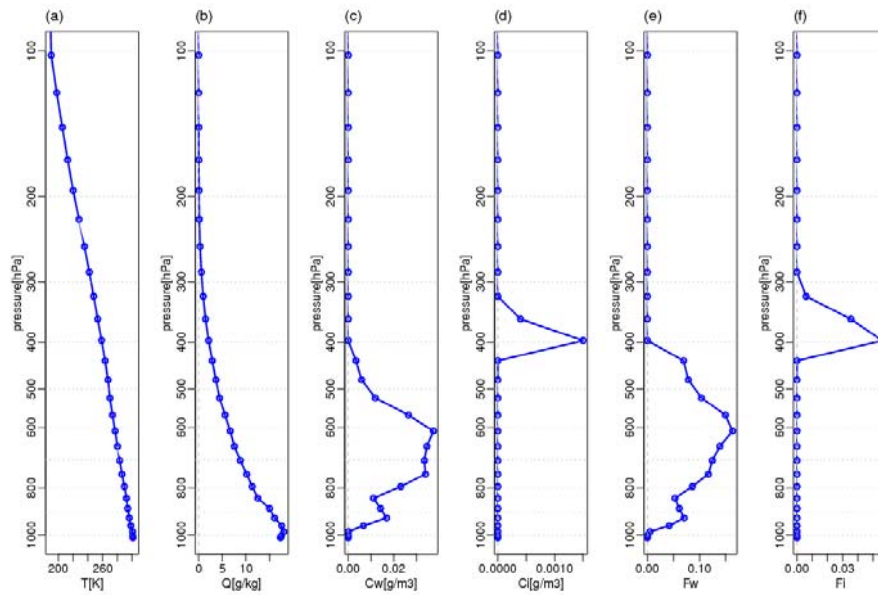
Figure 2.1 Background profile of (a) temperature, (b) humidity mixing ratio, taken from the first profile out of the 27 profile set. (c) cloud water content, (d) cloud ice content, (e) cloud water fraction, (f) cloud ice fraction, calculated from the temperature and humidity.
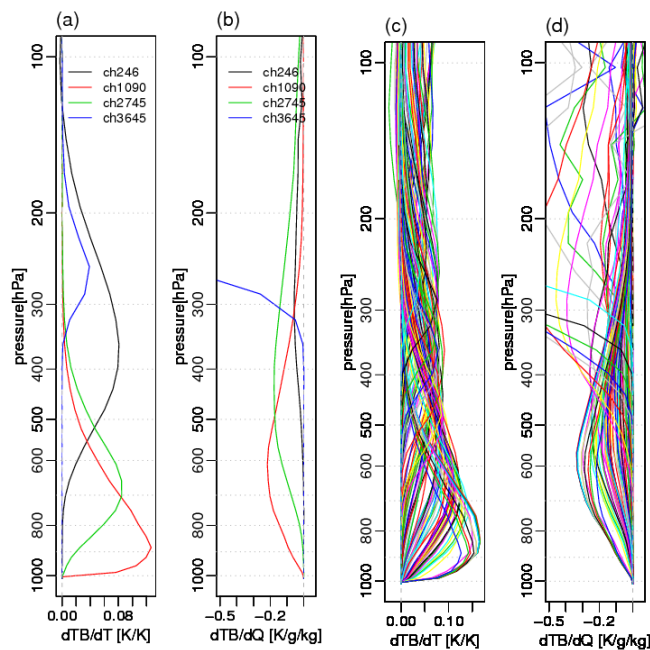
Figure 2.2 Temperature and humidity Jacobian of the profile in Fig.2.1for (a, b) the basic channel set, and (c, d) the quasi operational 141 channel set.
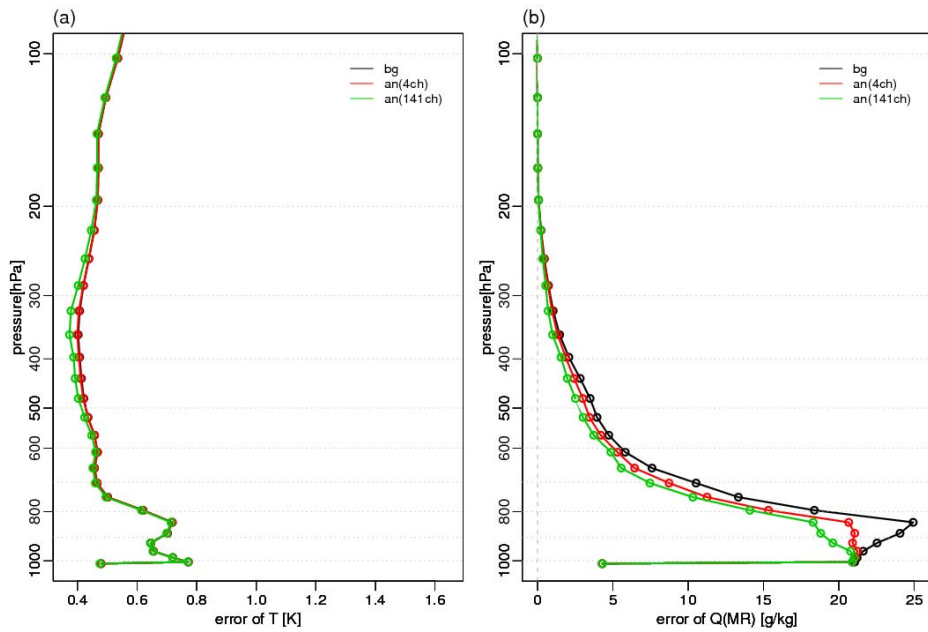
Figure 2.3 (a) temperature background error (black), analysis error with 4 ch used (red), and analysis error with 141 ch used (green) of the profile in Fig 2.1. (b) the same as (a) but for humidity.
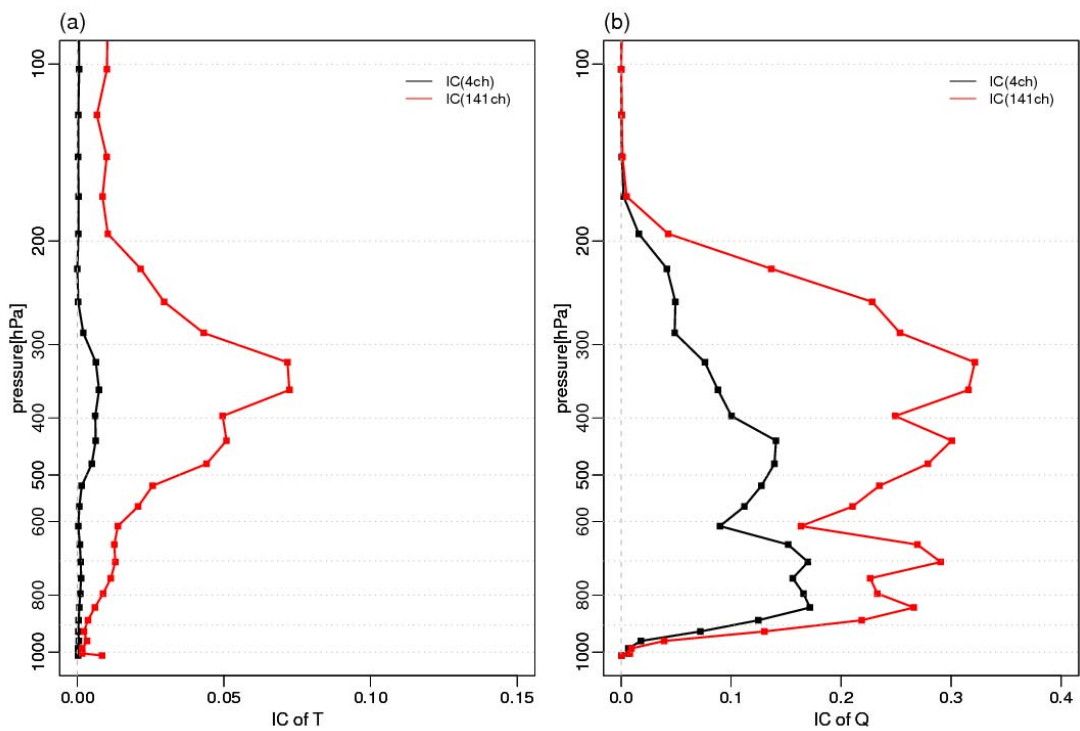
Figure 2.4 (a) Information contents (ICs) of temperature using 4 channels (black lines) and 141 channels (red). (b) The same as (a) but for humidity.
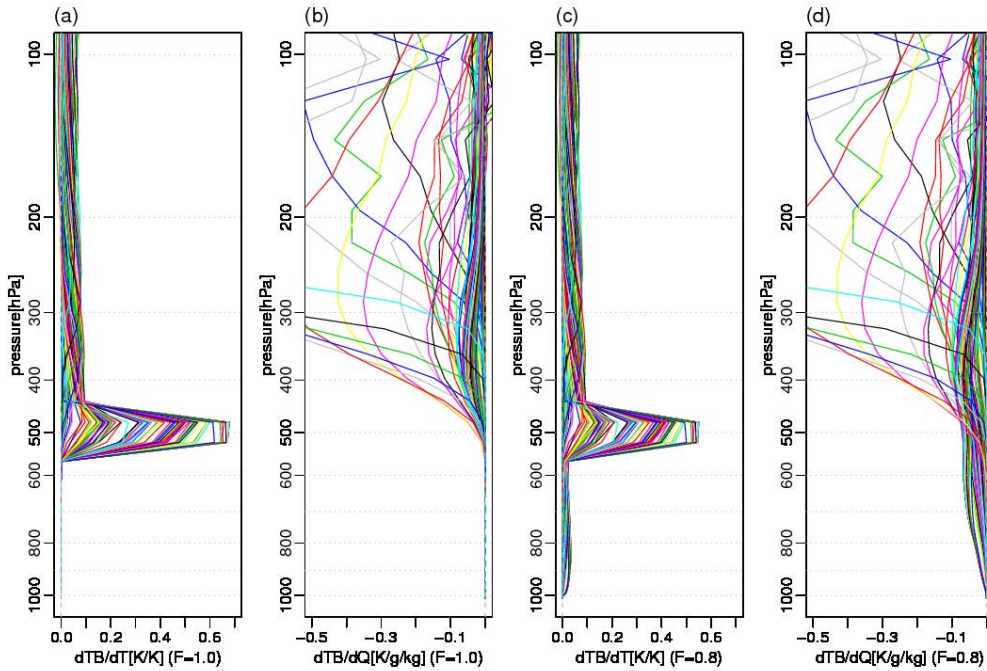
Figure 2.5 (a) temperature Jacobians of 141 channels for single-layer cloud of P_c=500 hPa and F=1.0, (b) mixing ratio Jacobian, (c, d) the same as (a, b) but for F=0.8.
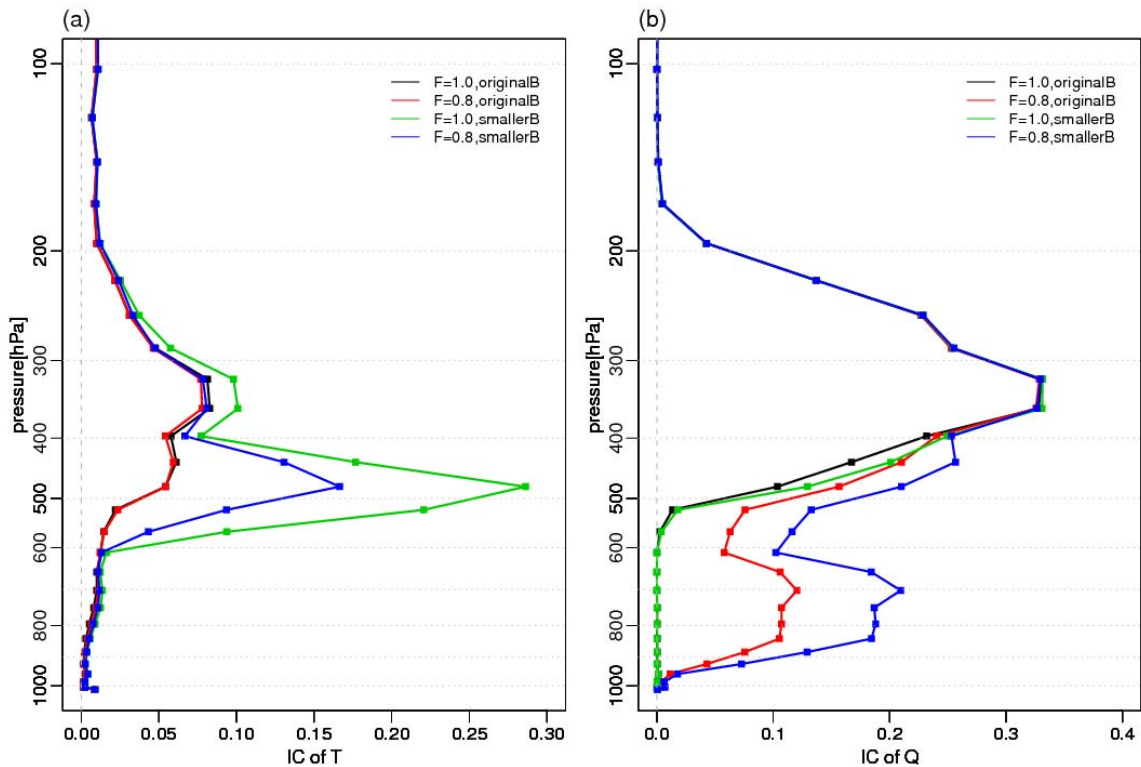
Figure 2.6 Temperature and humidity ICs for single-layer cloud of cloud top pressure $C_p = 500$ hPa and cloud fraction $F = 1.0$ (black) and $F = 0.8$ (red) with original cloud background error variance (30hPa and 0.1). ICs with smaller cloud background error variance (3hPa and 0.01) are
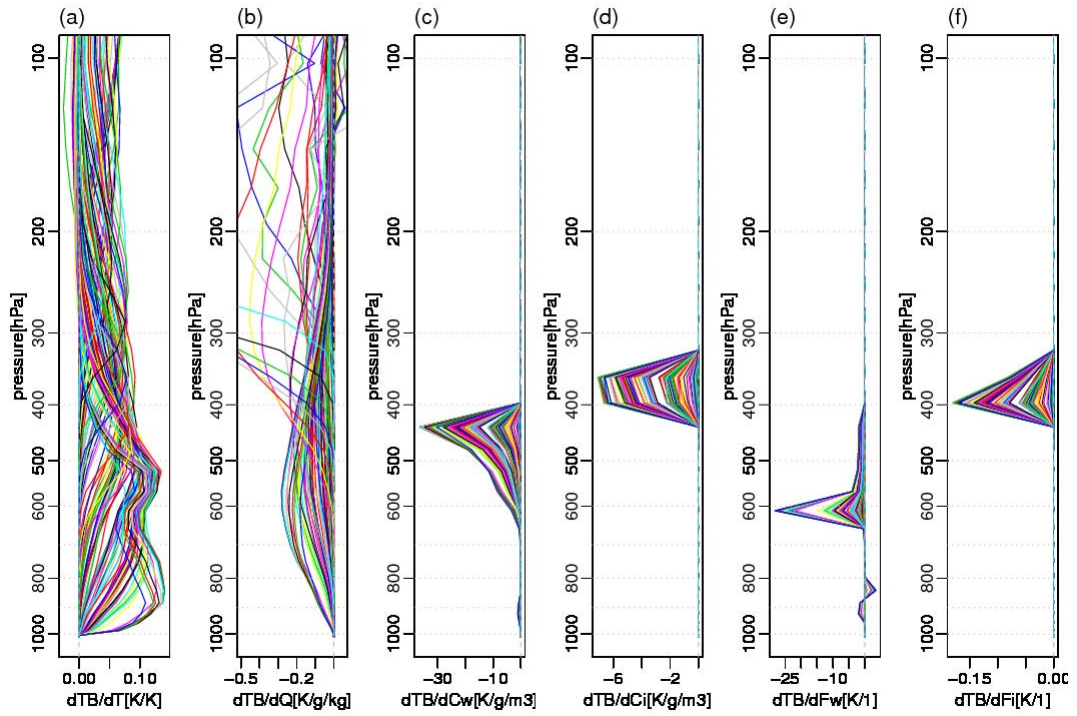
Figure 2.7 141 channel Jacobians with respect to all variables of multi-layer clouds in Fig 2.1.
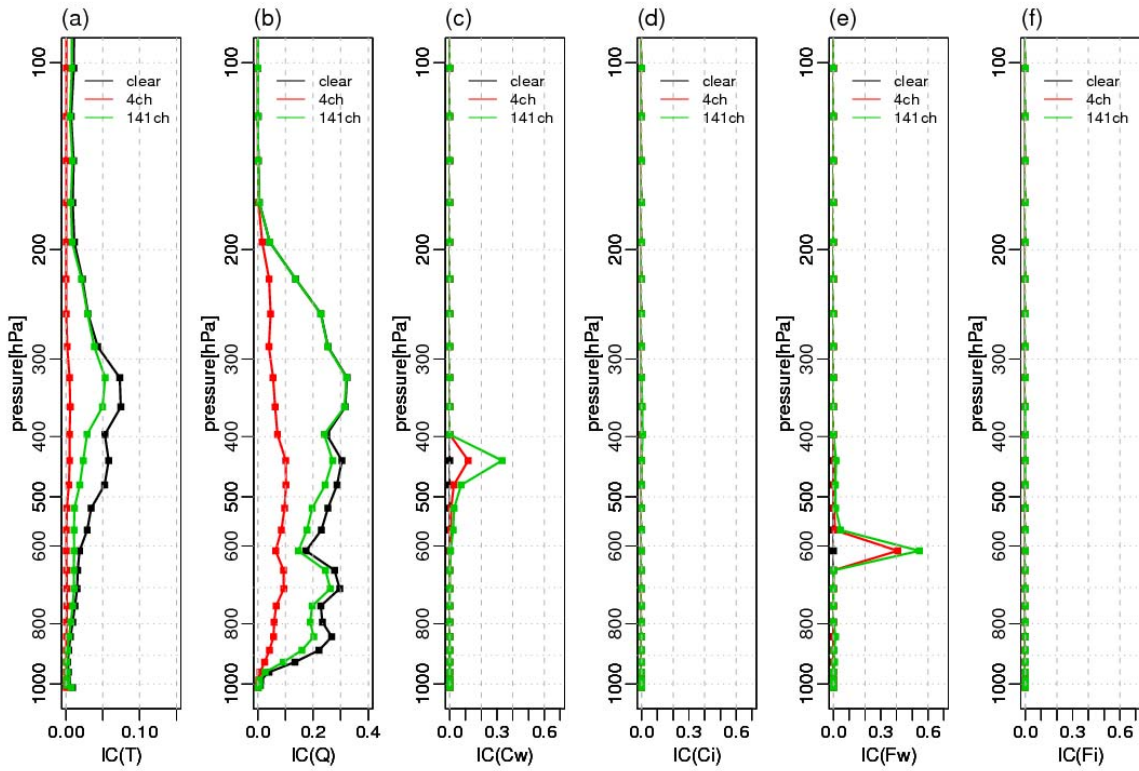
Figure 2.8 ICs corresponding to the Jacobians of the multi-layer cloud in Fig.2.7 with 4 channels used (red) and 141 channels used (green). For reference, ICs with 141 channels in the clear-sky case are also plotted (black).
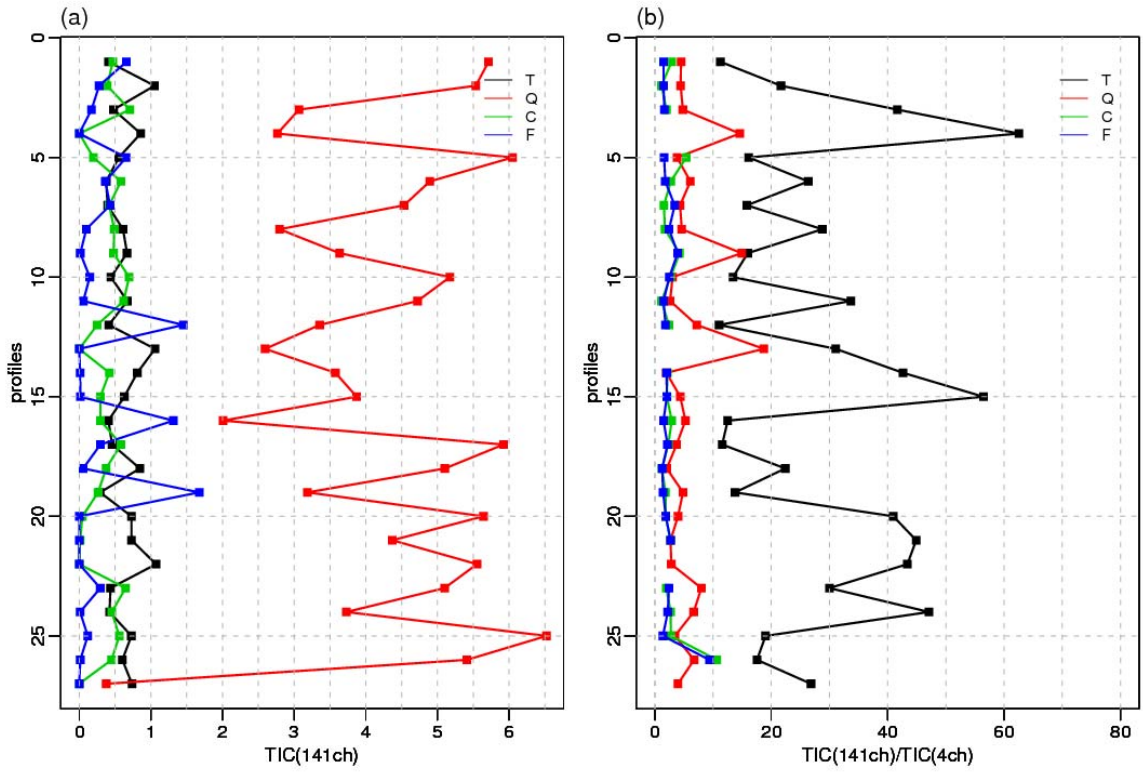
Figure 2.9 Total ICs (TIC) of temperature, humidity, cloud content and fraction for 27 profiles. (a) TICs using 141 channels. (b) Ratio of TICs with 141 channels to TICs with 4 channels.
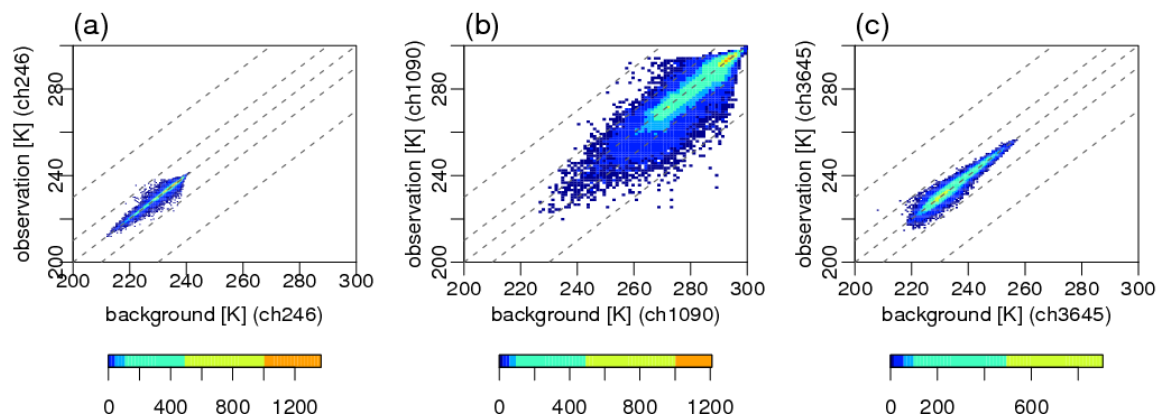
Figure 3.1 The density scatter plots of background and observation brightness temperatures (BTs) at channels 246, 1090 and 3645. The data are taken from the globe over the sea from 1 to 13 August 2011. Dashed lines represent observation-minus-background (O–B) = ±10K and 30 K.
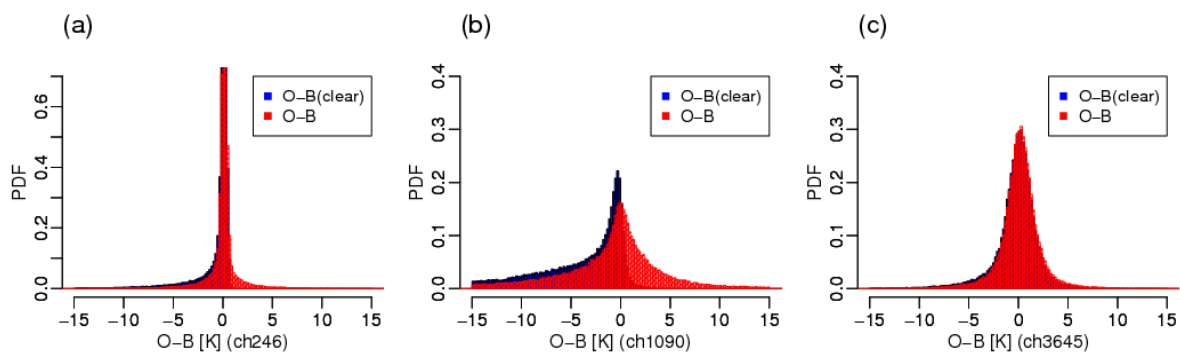
Figure 3.2 PDFs of O–B when the cloud scattering effect is switched on (red) and off (blue). The data use are the same as Fig 3.1
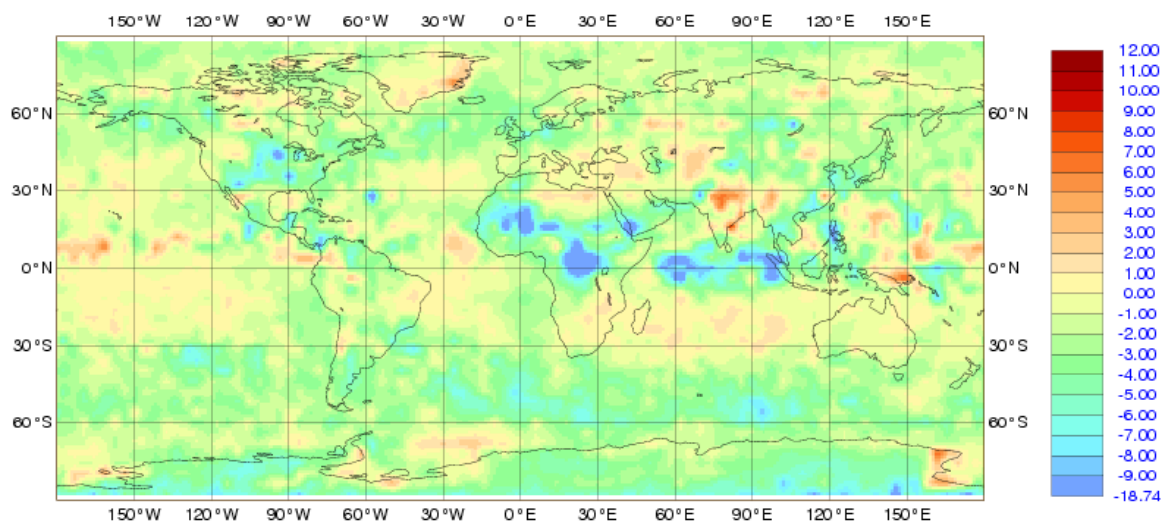
Figure 3.3 Monthly mean of O–B at channel 1090 calculated in 4 degree box of the data from 1 through 31 August 2011.

(a)

(c)
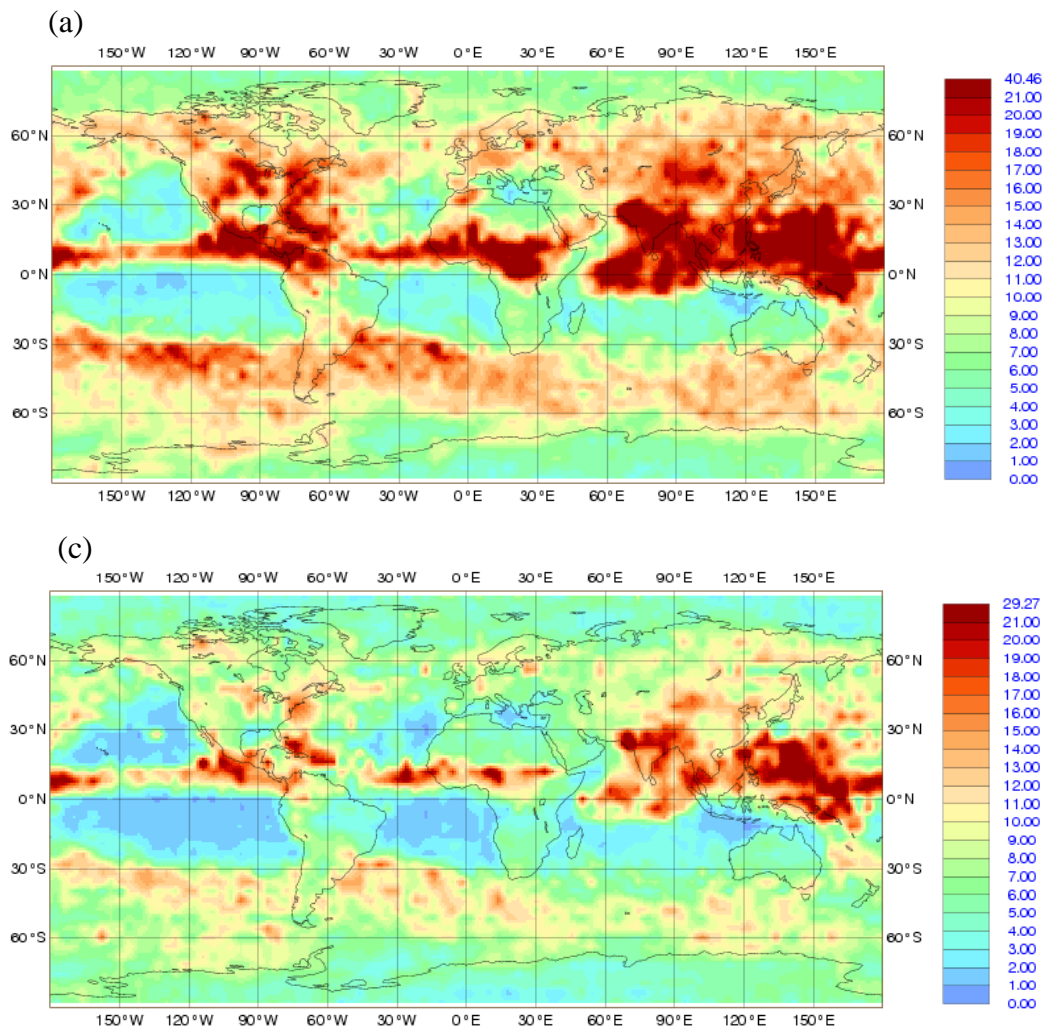
Figure 3.4   Monthly O–B SD of observation (a) and background (b) at channel 1090.
The data is the same as Fig. 3.3.
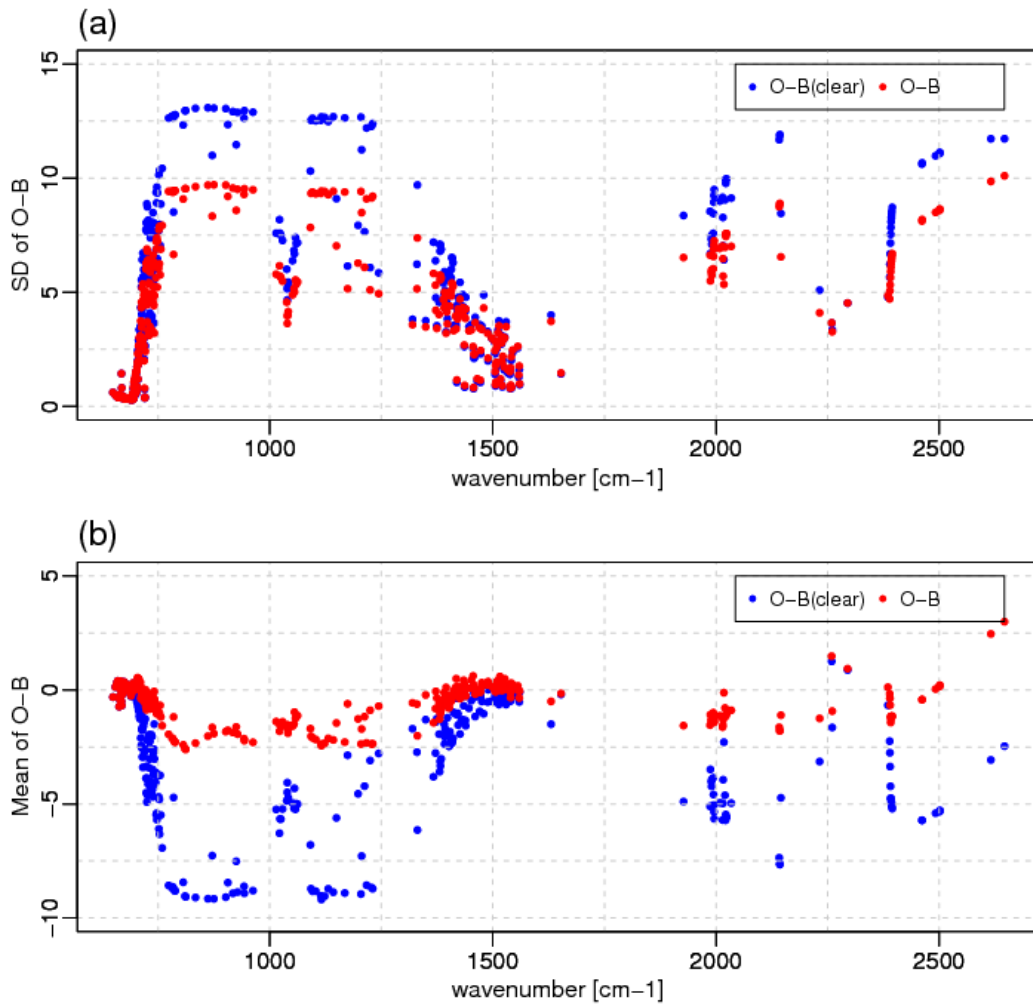
Figure 3.5 (a) SD and (b) mean of monthly O–B at 373 channels when the cloud scattering effect is turned off (blue symbols) and on (red) in RTTOV.
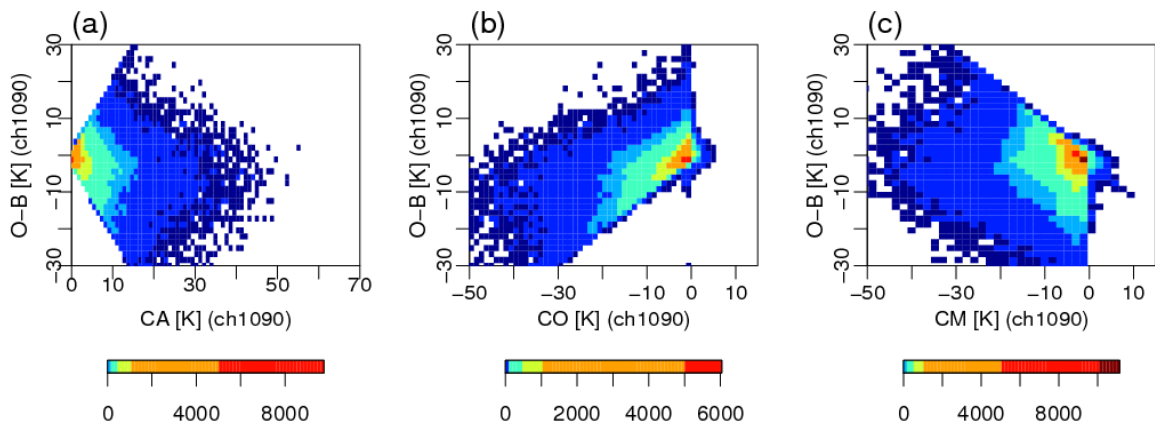
Figure 3.6 Density scatter plot of O–B against (a) cloud effect average (CA), (b) cloud effect for observation (CO) and (c) cloud effect for model (CM) at channel 1090.
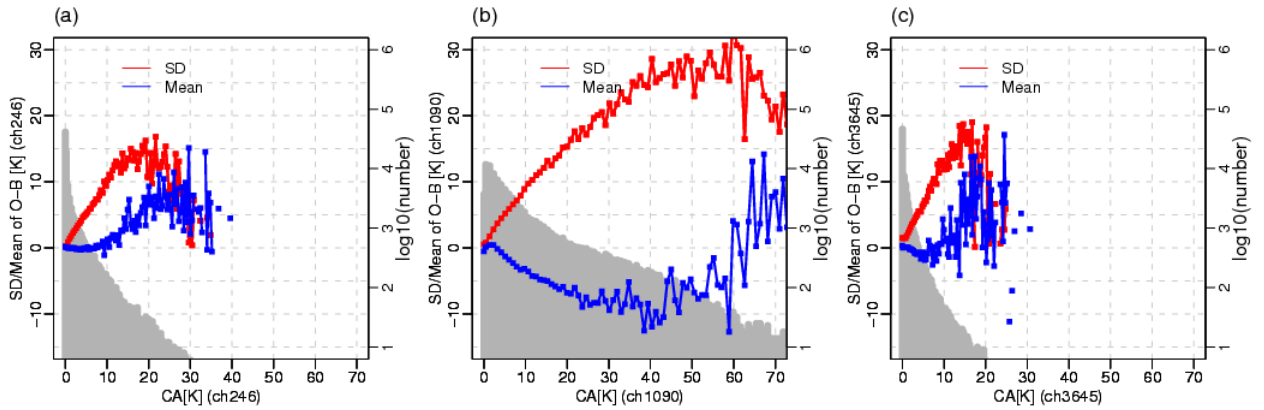
Figure 3.7 Mean (red) and SD (blue) of O–B at (a) channel 246, (b) channel 1090, and (c) channel 3645 as a function of CA. The sample number in each CA bin is shown with grey bars in the right axis.
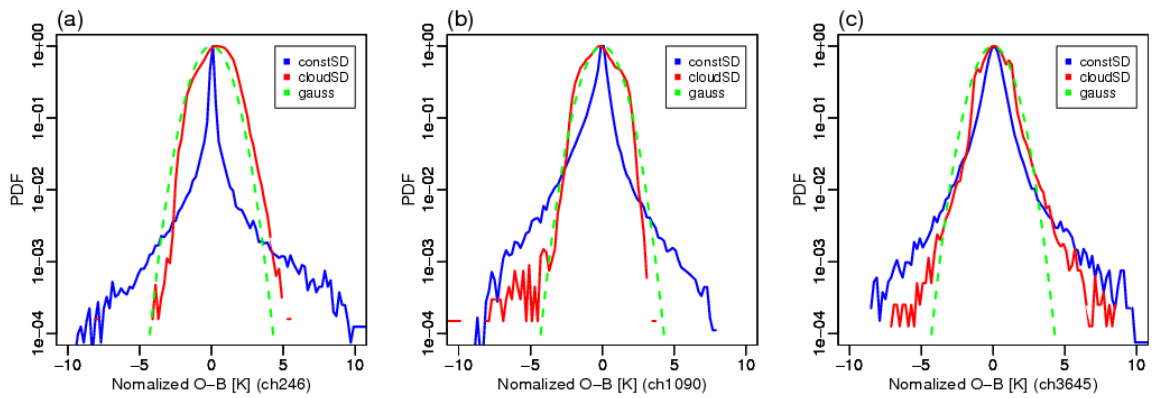
Figure 3.8 PDFs of O–B normalized by O–B SD. SDs calculated from the whole sample, in which SD is constant (blue lines), or estimated as a function of CA (cloud-dependent SD, red). The vertical axis is taken in log scale. Normal Gaussian PDFs are also plotted with green dashed line.
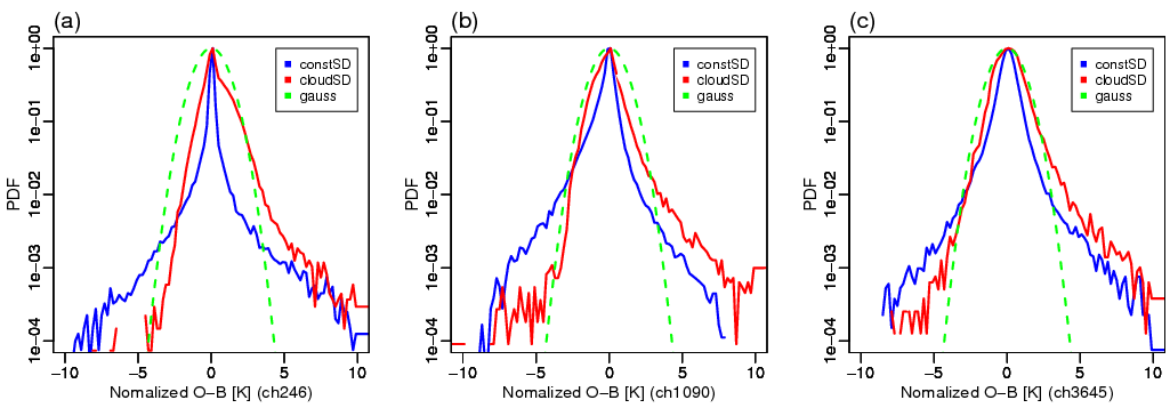
Figure 3.9 The same as Fig. 3.8 but O–B normalized by O–B SD as a function of CO.
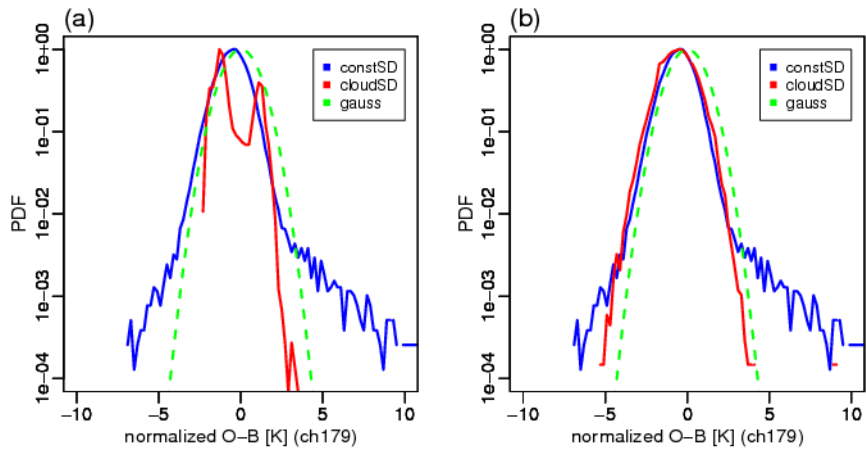
Figure 3.10 (a) Normalized O–B at channel 179 taking into no account minimum O–B SD, (b) The same as (a) but set clear-sky O–B SD to the minimum.
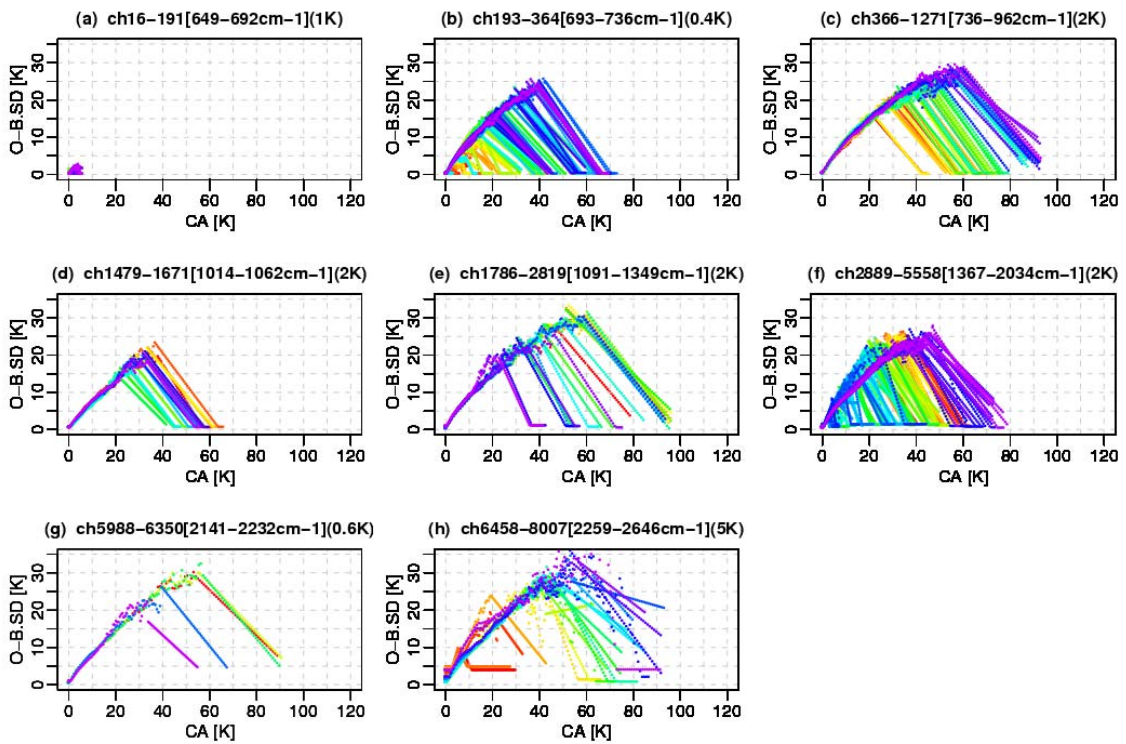
Figure 3.11 O–B SD of all 373 channels as a function of CA, taken from the look-up-table (LUT, see the text). The data samples are taken from the globe over the sea from 16 to 31 August 2011
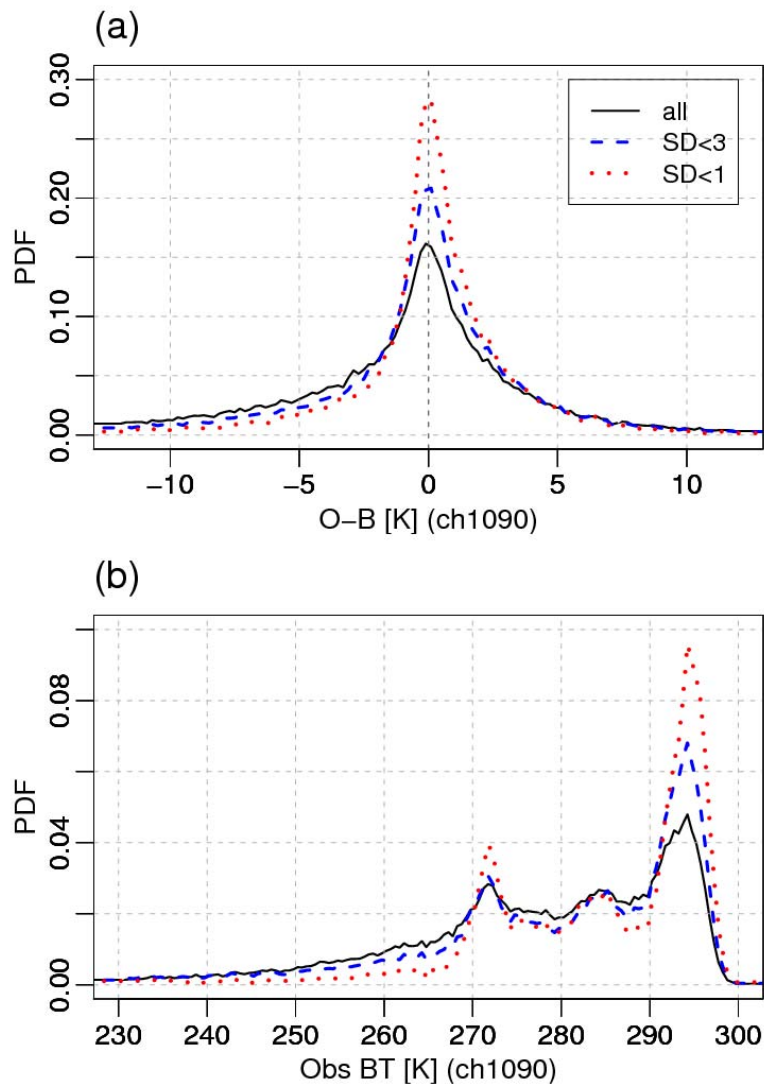
Figure 3.12 (a) PDFs of O–B for samples with $SD_{AVHRR} < 1.0$ [mW/m^2/sr/cm^{-1}] (dotted line), $SD_{AVHRR} < 3.0$ (dashed line) and all data (solid line). (b) The same as (a) but for PDF of observed BT.
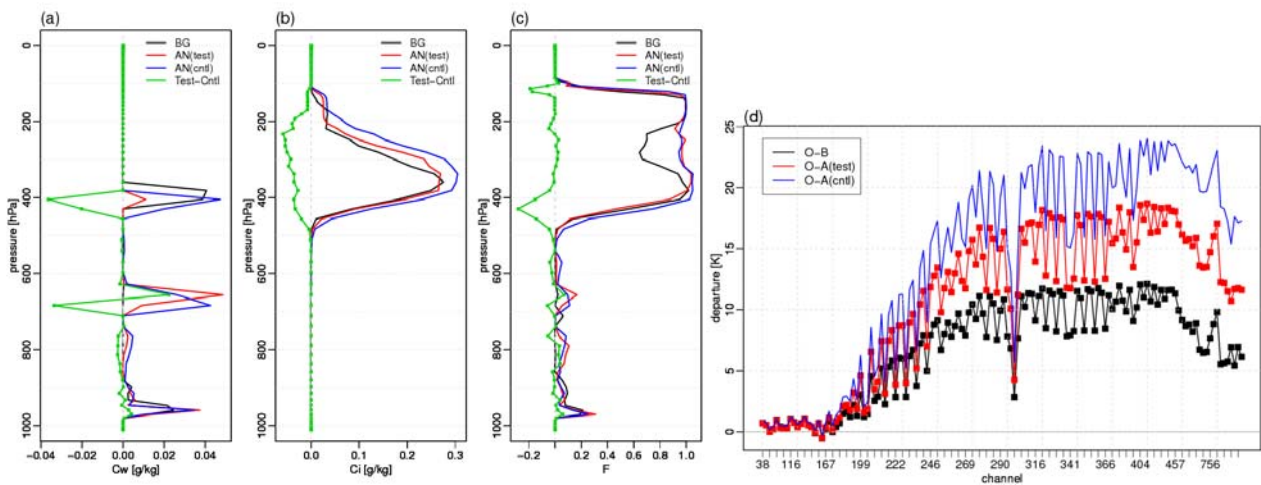
Figure 4.1 (a,b,c) Cloud water content (C_w), cloud ice content (C_i) and cloud fraction (F) profiles for FG (black lines), TEST analysis (red), CNTL analysis (blue), and analysis difference between TEST and CNTL (green) for case 1 experiment. (d) O-B (black lines with squares), O-A of TEST (red lines with squares) and O-A of CNTL (blue lines) of channels used in TEST for case 1 experiment. experiment.
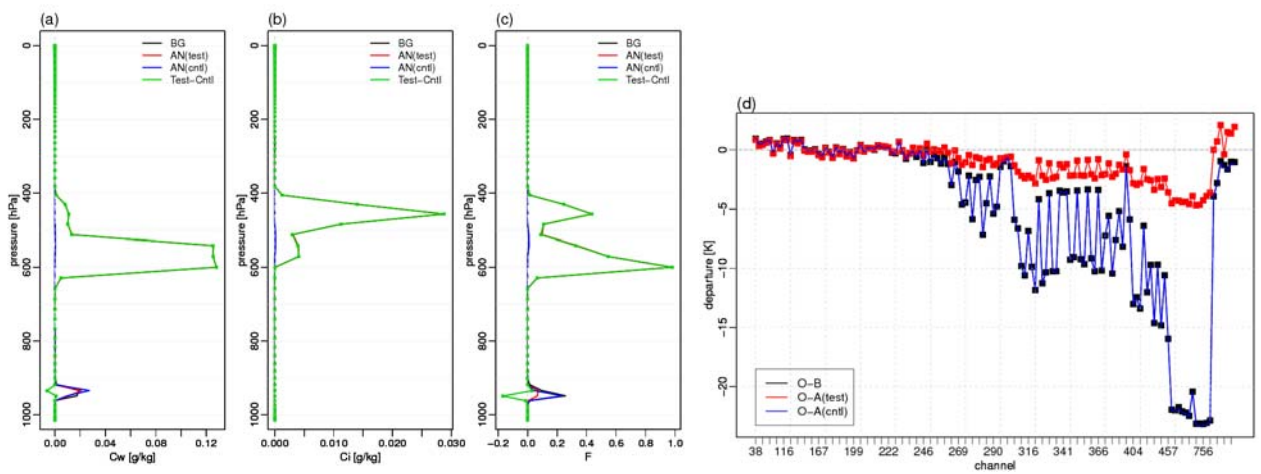

Figure 4.2 The same as Fig. 4.1 but for the case 2 experiment. Please note that in (a, b, c) black lines of FG and blue lines of CNTL analysis are at almost zero of clouds, and that red lines of TEST analysis are overwritten by green lines of analysis difference.
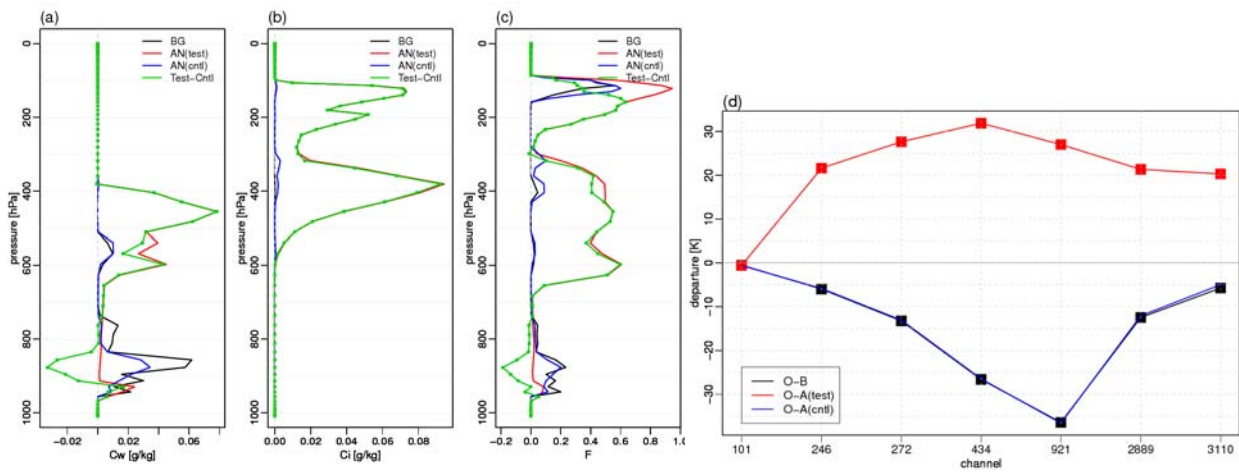
Figure 4.3 The same as Fig. 4.1 but for the case 3 experiment.
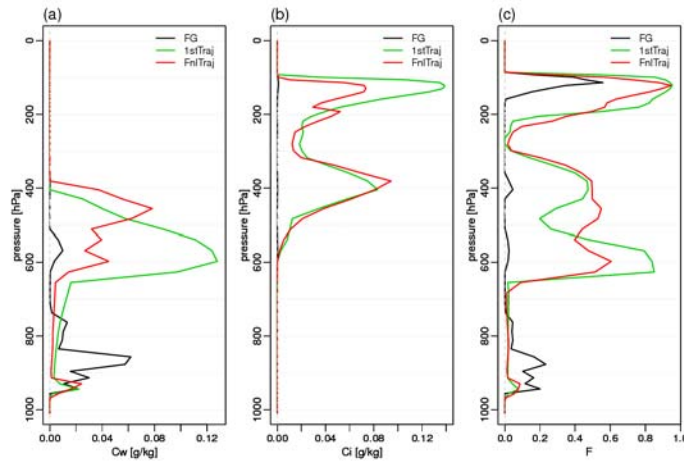
Figure 4.4 Cloud profiles of FG (black lines), first updated trajectory of TEST (green), and final trajectory of TEST (red) for the case 3 experiment.
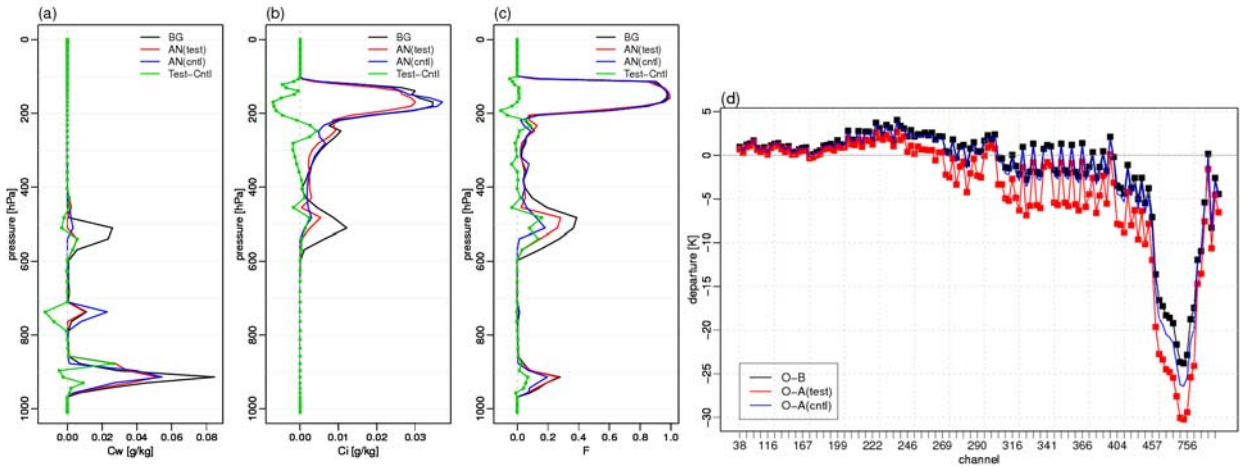
Figure 4.5 The same as Fig. 4.1 but for the case 4 experiment.
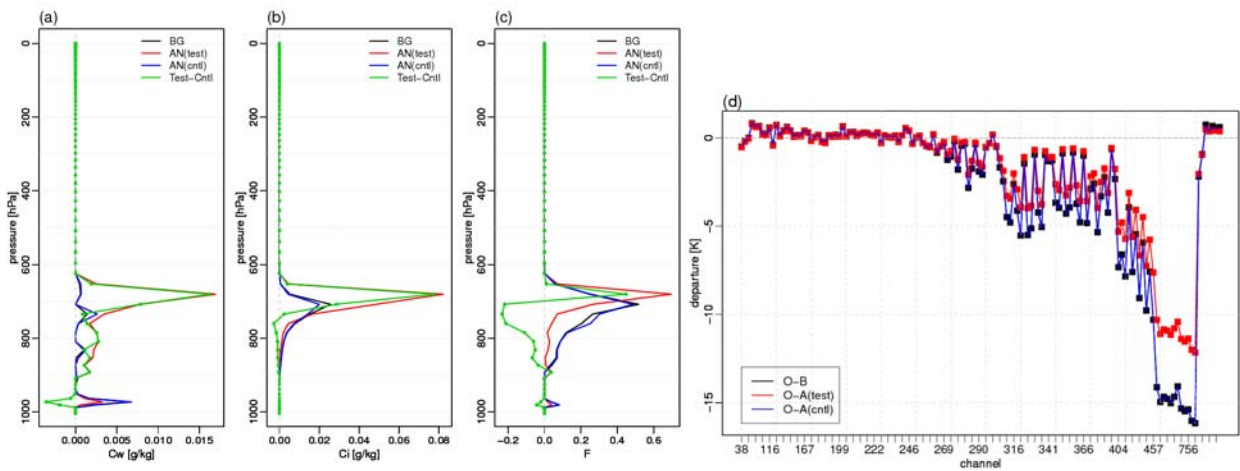
Figure 4.6 The same as Fig. 4.1 but for the case 5 experiment.